STUDY OF EFFECTS ON THE WING'S AERODYNAMIC CHARACTERISTICS DUE TO DISTRIBUTED PROPULSION OVER WINGSPAN

Gustavo Jorge Resende[1], Dr. Vinicius Malatesta[1], Eng. Marcos César Savio[2] & Eng. Dr. Breno Moura Castro[2]

[1] Aeronautics Institute of Technology, São José dos Campos, SP, 12228-900, Brazil
[2] EMBRAER, São José dos Campos, SP, 12227-901, Brazil

Abstract

Distributed propulsion (DP) is not a new concept but recent advances in electric motors and batteries, along with the need for more environmentally friendly products, brought this concept back to the spotlight. This paper addresses two types of DP: wingtip-mounted propellers and distributed propellers along the wingspan. The benchmark of the analysis is NASA's X-57 "Maxwell" demonstrator. Another goal of this paper is to evaluate how good is the VSPAERO code to modeling aerodynamic flows, from a simple case of the isolated wing to a more complex 14 rotors case. The overall results show that VSPAERO provides good estimations for most cases.

Keywords: VLM; Distributed-Propulsion; High-Lift Propellers; VSPAERO

1. Introduction

1.1 Motivation

The technological breakthroughs achieved by the electric motors industry in the past years, pushed by the need for more environmentally friendly sources of energy, allowed this type of solution to be considered in the latest aircraft designs. Due to the scalability of electric motors, the new aircraft designs that adopt electric propulsion benefit from great variety and flexibilization of configurations and parameters, which were not technically viable in a design with conventional combustion engines. Besides, electric motors have a simpler architecture than combustion engines and fewer moving parts, which improves the system's reliability and reduces noise signature.

The use of small electric motors and propellers placed along the wingspan is a type of Distributed Electric Propulsion (DEP) enabled by the formerly mentioned characteristics of electric motors. These systems can improve the dynamic pressure over the wing and its stall characteristics, enabling the use of simpler high-lift devices [1]. In addition, this allows the wing design optimization to be constrained by cruise requirements and less by takeoff and landing [2, 3], which directly affects the wing area sizing.

That is only one of the many reasons the topic of DEP came into the spotlight in the aeronautical industry and research in the last years. Hence, it is relevant to understand how this kind of configuration affects an aircraft design.

1.2 Objectives

One of the goals of the present work is to study the effects that distributed propulsion (DP) has on the wing's aerodynamic characteristics. This study will be conducted using mid-fidelity methodologies, based on potential flow theory. The software chosen to apply such methodologies is the Open Vehicle Sketch Pad (OpenVSP) [4], along with its embedded analysis tools.

At first, a verification of the OpenVSP software and its aerodynamic solver capabilities, the VSPAERO, is evaluated. The benchmark of such analysis is the NASA's X-57 "Maxwell" demonstrator, which

was chosen because of the extensive literature and available data related to it. In addition, such comparison will contribute to establish best practices of simulation within this software.

Since the VSPAERO will perform all simulations, another goal here is to evaluate how good this solver is in computing the flow field of a wing, especially when several propellers are present. The propellers are modeled with the *Actuator Disk Mode*. Later on, this model will be discussed in detail, but one of its main advantages is that it adds low computational costs to the solver. Thus, if the results are reasonable enough, this could mean that it is viable to apply VSPAERO to early design phases, where the compromise between computational cost and precision is of great importance.

In addition to the solver performance, it is relevant to evaluate how easy it is to extract the output data and export it to other codes for further analysis or to improve some calculations. For example, the parasite drag integration mentioned in section 3.2 uses some output data from VSPAERO to provide a better estimation of the wing parasite drag.

Finally, a parametric study will be performed regarding different geometric parameters for the propellers distributed along the wing's leading edge. This study will aim to build a better understanding of how the parameters affect the wing's aerodynamics and to explore what flow-field phenomena the actuator disk model present on VSPAERO can capture or not.

1.3 The X-57 "Maxwell" Model

The X-57 "Maxwell" is a demonstrator of the DEP technology, developed by NASA's Scalable Convergent Electric Propulsion Technology Operations Research (SCEPTOR) project. Its main purpose is to demonstrate how DEP can contribute to increase energy efficiency and performance when compared with its baseline aircraft [5]. Also, the X-57 will provide background on standards and regulations related to DEP technology.

Its development started from a baseline GA aircraft, the TecnamP2006T, powered by a conventional combustion system. Then, its design passed through different phases (or "Mods" as it is referred to in most X-57 papers). The final version (Mod IV) reached an incredibly 58% reduction in wing area (Fig.1), which is one of the main contributors to the increase in energy efficiency mentioned earlier. It employs two different types of DP concepts with 14 electric motors [6], and such reduction is indirectly enabled by the 12 propulsors distributed along the wing's leading edge. These small foldable propellers are designed to operate during the low-speed phases of the mission and to largely improve the aircraft stall characteristics by augmenting the low-speed flowfield over the wing [6]. Such configuration enables the wing project to be directed by cruise phases constraints, which usually "accepts" smaller wing areas. Hence, the smaller the area, the smaller the wing drag.
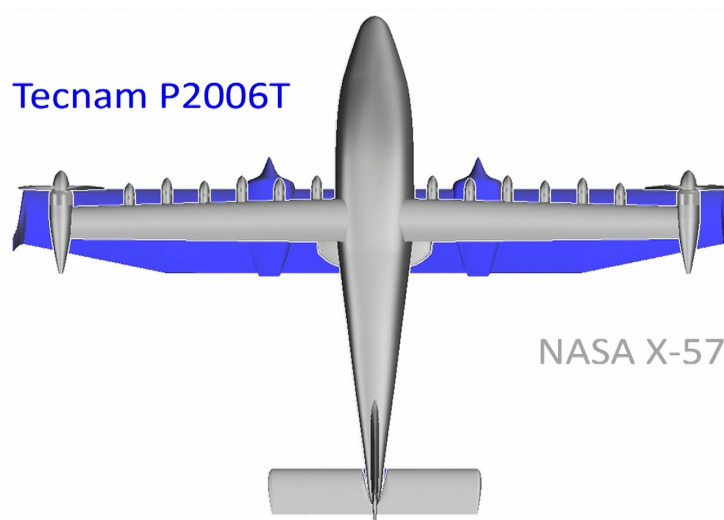
Figure 1 – Top view comparing the X-57 and the Tecnam P2006T planforms. Source: [7].

The two remaining propulsors comprise large wingtip-mounted propellers, used as the main propulsive power at all mission phases. Unlike the 12 smaller propellers, the wingtip ones have variable-pitch to maintain their efficiency through the different flight phases. Their rotation is opposite to the

wingtip vortex, resulting in a reduction of the wing induced drag [8].

In addition to all literature available regarding the X-57 demonstrator, its geometrical model is also available on the OpenVSP Hangar [9]. The OpenVSP Hangar is an online database website where users can share their models with the community. This model was used throughout this work, and besides the mesh refinement and change in units (to pass the model from inches to feet), no modifications were made. Table 1 brings the reference lengths used in the aerodynamic solver for the X-57 wing.

Table 1 – Reference lengths for the X-57 "Maxwell".

Parameter	Symbol	SI units		Imperial units	
Area	S_{ref}	6.194	[m^2]	66.667	[ft^2]
Span	b_{ref}	9.639	[m]	31.623	[ft]
Chord	c_{ref}	0.643	[m]	2.108	[ft]

2. Technical Foundation

The analysis conducted in this work consists of low and mid-fidelity aerodynamic models of flow-fields. This means that grid-based Computer Fluid Dynamics (CFD) methods, resolving or modeling the complete formulation of the Navier-Stokes equations, are out of the scope of this project. Many literature regarding aerodynamic basics [10, 11, 12] were consulted. Special attention is given to the book of Professor Mark Drela [13] where he details the technique of velocity field modeling via source and vorticity fields. This reference also outlines concepts of force analysis, drag decomposition, and flow interference estimation, which contributes to an intuitive understanding of aerodynamic flows.

Furthermore, a fair amount of research was dedicated to propeller modeling. Reference [14] summarizes the classical methods of rotor modeling, from the simplest ones as the Momentum Theory (also known as Actuator Disk) to the more complex ones as the Momentum-Blade Element Theory and the methods that use Vortex Theory.

The interaction between the wing and the propellers is also a vast field of research. Reference [15] provides a theoretical background on this topic, as well as numerical and experimental data involving a wide range of aircraft geometry and flow condition parameters. References [8] and [16] also approach the wing-propeller interaction, but they focus specifically on the tip-mounted propellers configurations. Finally, Ref. [3] addresses the interaction of the wing with high-lift propellers along the wingspan and develops a simplified model that estimates lift augmentation from such propellers. This simplified model, based on thin wing theory and the impacts of the propeller slipstream on dynamic pressure and circulation, provides a good intuition about the numerous parameters of a propeller installation (e.g., diameters, angles, and location on the wing) and on how they can affect a wing design.

Since VSPAERO is the analysis tool used for all simulations in the present work, which has an open-source code, it is relevant to discuss and understand the particularities of the models built in this software. Thus, the following sections will present the equations of the lifting surface and actuator disk models implemented in VSPAERO. Also, some of the analyses leveraged the unsteady mode available in the software, so it will also be briefly discussed.

2.1 Lifting-surface Problem Formulation

VSPAERO, developed by David Kinney, is the solver used to perform all 3D aerodynamic simulations. Despite the lack of documentation available about the software, at the OpenVSP Workshop of 2020, [17] presented the theory, features, and validations behind VSPAERO. The program has the VLM and Panel Method implemented, but only the first will be discussed here. Although the Panel Method can capture airfoil thickness effects, which is neglected by the VLM, it is much more time-consuming. As long as the wing geometries being analyzed are relatively thin (t/c less than 12%, approximately), the increase in "accuracy" provided by the Panel Method would not justify its use.

2.1.1 Vortex Placement and Boundary Conditions

An interesting feature of OpenVSP is the link between the geometry resolution and the mesh refinement that will be used by the aerodynamic solver. The 3D geometry can be easily transformed to a 2D camber surface, which is analog to the 2D vortex sheet that represents the wing geometry within the aerodynamic solver. This camber surface will have the same number of control points along the chord and span directions as the original geometry. Moreover, the spanwise elements at the trailing edge tells VSPAERO the number of elements representing the wake aft the trailing edge.

Because of this interchange between the OpenVSP geometry and the VSPAERO mesh, it is natural that it might be composed of triangles, quadrilaterals or any general "N-sided" polygons [17] depending on the geometry complexity. To leverage this variety of polygons present in the mesh, the singularities used by the aerodynamic solver are vortex rings with the respective shapes of the mesh elements (see Fig. 2). The strength of those vortices are determined respecting the flow tangency condition. Particularly in VSPAERO, this condition is determined in the vortex ring centroid.

The shed wakes are "modeled as vortex lines leaving the sharp trailing edges of wings"[17]. The strength of these vortex lines is determined by the application of the Kutta Condition [10, 11, 13]. In VSPAERO, by default, the wake lines are not fixed, and their position is iteratively solved with the field velocity solution in such a manner that they will also represent the field streamlines [17]. According to [18], solving for the wake-flow behavior improves significantly results when there are other surfaces behind the wing "wet" by the wake because it will directly affect the effective angle of attack "seeing" by the aft surfaces.

It is worthy to point out that in a traditional VLM [13, 14], the singularities placed over the wing geometry usually are horseshoe vortices, forming a regular structured mesh. Figure 2 illustrates such differences between the "conventional" VLM and the VSPAERO meshes. This is one of the reasons that some researchers argues that this mode of VSPAERO is not technically a VLM. According to the definitions presented by [18], the approach implemented in VSPAERO is a Lifting Surface Method.
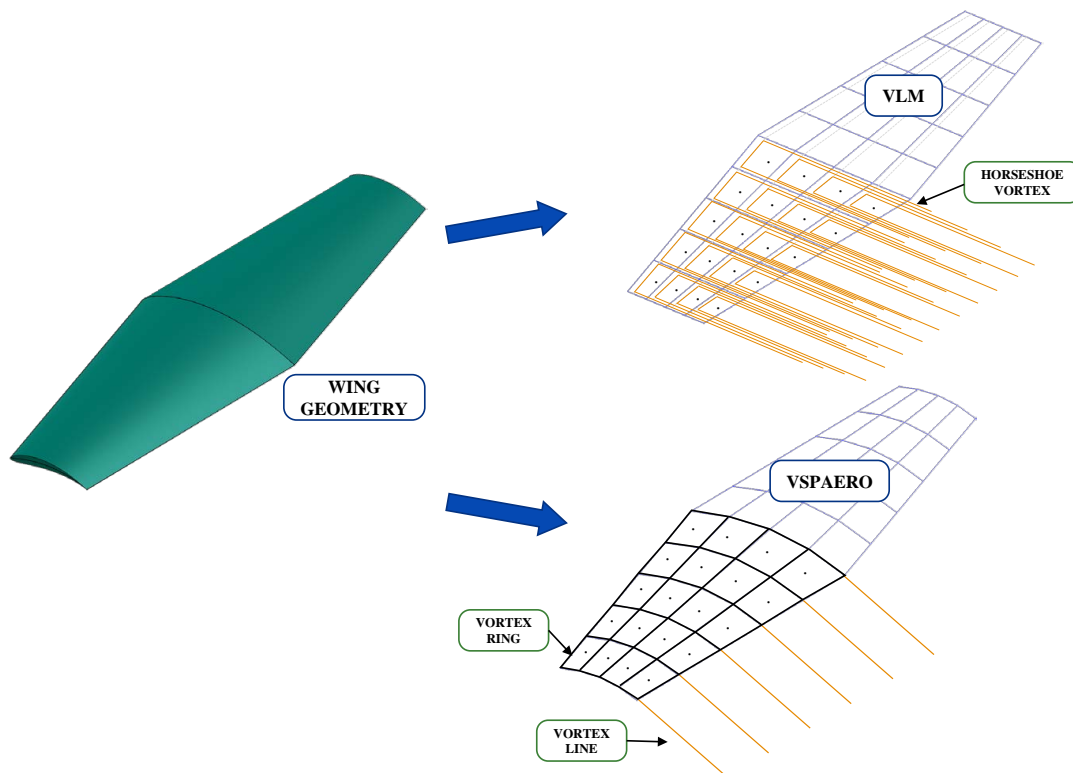
Figure 2 – Comparison between the horseshoe vortices from VLM and the vortex ring and lines positioning from VSPAERO.

2.1.2 Problem Formulation and Boundary Conditions

Once the vortex rings and wake filaments are defined, the next step would be to calculate the velocity induced ($\vec{V}_P$) by each vortex segment in a given control point (P), as illustrated in Fig. 3.
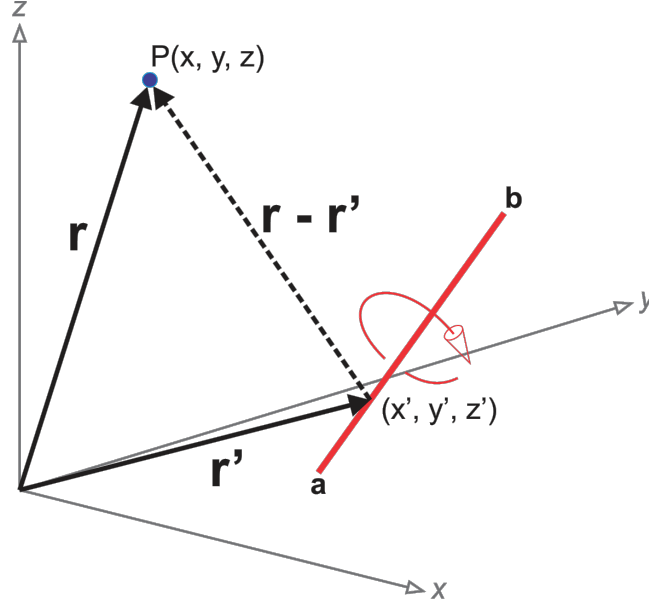
Figure 3 – Representation of a 3D straight vortex segment, and geometry definition used to evaluate its induced velocity in a given point P. Adapted from Ref. [13].

This induced velocity is modeled in VSPAERO using the generalized Biot-Savart law [17]:

$$\vec{V}_P = \frac{-\beta}{2\pi K} \cdot \int_a^b \frac{\vec{\Gamma} \times [\vec{r} - \vec{r}']}{r_\beta{}^3} ds \tag{1}$$

where $\beta = \sqrt{1 - M_\infty{}^2}$ is the *Prandtl-Glauert factor*, and K is a factor to account for compressibility effects on the formulation. If M_∞ is less than one, then $K = 2$, otherwise $K = 1$. Finally, r_β is defined by the following expression:

$$r_\beta{}^2 = (x - x')^2 + \beta^2 \left[(y - y')^2 + (z - z')^2 \right] \tag{2}$$

Note that, Potential Flow Theory does not account for compressible flows. However, it is possible to apply corrections and assumptions to the original formulation in order to model compressibility effects. Reference [13] approaches this subject more deeply. Also, it is easy to see that if the flow is incompressible ($M_\infty = 0$), equations (1) and (2) reduces to the simpler form of the Biot-Savart law. Then, at the centroid of a given vortex ring i, the induced velocity from all other rings and trailing wakes is given by:

$$\vec{V}_i = \sum_j^{N_{rings}} \vec{V}_{ring_j} + \sum_j^{N_{wakes}} \vec{V}_{wake_j} \tag{3}$$

As mentioned before, the strength of the vortices (Γ_i) are the only unknowns and are determined respecting the flow tangency condition. Particularly in VSPAERO, this condition is determined in the vortex ring centroid [17]. In addition to the induced velocity from the vortex rings and wake, the tangency condition also considers the free stream velocity and the total velocity induced from any rotors.

$$\left[\vec{V}_\infty + \vec{V}_{rotors} + \vec{V}_{wakes} + \vec{V}_i \right] \cdot \hat{n}_i = 0 \tag{4}$$

Rearranging Eq. (4) leads to a NxN linear system for each unknown Γ_i, where N is the number of vortex rings in the mesh.

$$\boldsymbol{A} \cdot \vec{\Gamma} = \vec{b} \tag{5}$$

There are a variety of methods to solve this kind of linear system, which can be either direct solver or iterative solvers. Due to the possibility of modeling complex geometries in OpenVSP, a direct solver would cause expanse computational costs to VSPAERO. For this reason they implemented an iterative solver, using a technique of Preconditioned GMRES (Generalized Minimal Residual) of Saad-Schults. In addition to this, VSPAERO implements a series of techiques to speed up the convergence process of the linear system solution. However, these runs out of the scope of the present work.

Once the linear system is solved, the algorithm finally computes the aerodynamic forces and moments.

2.2 Actuator Disk - Improved Modeling

Among the many propeller models available in the literature [14], VSPAERO implemented an improved version of the Actuator Disk Theory. Using Conway's elliptic actuator disk model [19], VSPAERO is able to compute axial and radial velocities, and the pressure jump across the disk. In addition, it is also implemented Johnsons's actuator disk model [20], which provides tangential velocity.

VSPAERO manages to evaluate theses velocities with typical inputs. While modeling the propeller, within the OpenVSP environment, the user provides the rotor radius, position and thrust direction. Then, in VSPAERO's input section the user must provide values of thrust coefficient ($C_T = T/(\rho_\infty n^2 D^4)$), power coefficient ($C_P = P/(\rho_\infty n^3 D^5)$), and RPM for each propeller.

2.2.1 Conway's Actuator Disk Model

Conway proposed an analytical method that solves, in closed form, the flow induced by a linearized propaller actuator disk with variable load distribution [19]. His work provides the formulation for different forms of load distribution and, as mentioned above, VSPAERO implemented the elliptic loading. According to [19], a propeller with radius R will induce an axial velocity in a point (r,z), where r is the radial coordinate ranging from 0 to R and z is the axial coordinate (so, the point (0,0) represents the center of the disk), respecting the following relations:

According to [19], the induced velocity in a point (r,z), where r is the radial coordinate ranging from 0 to R and z is the axial coordinate (so, the point (0,0) represents the center of the disk), by a propeller with radius R is given the following relations:

Axial Velocity

$$V_z(r,z) = 2.V_z(r,0) + v_i. \left\{ -\alpha + \frac{z}{R} \arcsin\left(\frac{2R}{\sqrt{z^2 + (R+r)^2} + \sqrt{z^2 + (R-r)^2}} \right) \right\}, \text{if } z \geq 0 \tag{6}$$

$$V_z(r,z) = \qquad v_i. \left\{ \alpha + \frac{z}{R} \arcsin\left(\frac{2R}{\sqrt{z^2 + (R+r)^2} + \sqrt{z^2 + (R-r)^2}} \right) \right\}, \text{if } z < 0 \tag{7}$$

Radial Velocity

$$V_r(r,z) = \frac{v_i \|z\|}{2r} \left(\frac{1}{\alpha} - \alpha \right) - \frac{v_i r}{2R} \left\{ \arcsin\left(\frac{2R}{\sqrt{z^2 + (R+r)^2} + \sqrt{z^2 + (R-r)^2}} \right) \right\} \tag{8}$$

Pressure jump across the Disk

$$\Delta P(r) = 2\rho_\infty V_\infty V_z(r,0) \tag{9}$$

In equations (6) to (9) it remains the definition of the following terms:

$$V_z(r,0) = \frac{v_i}{R}\sqrt{R^2 - r^2} \tag{10}$$

$$v_i = \frac{-V_\infty}{2} + \sqrt{\left(\frac{-V_\infty}{2}\right)^2 + \frac{T}{2\rho_\infty A}} \tag{11}$$

where T is the propeller thrust, obtained with the input C_T, and A is the frontal area of the disk. Finally, there is the factor α (not to be confused with the angle of attack):

$$\alpha = \sqrt{\frac{\sqrt{(R^2 - r^2 - z^2)^2 + 4R^2 z^2} + (R^2 - r^2 - z^2)}{2R^2}} \tag{12}$$

2.2.2 Johnson's Actuator Disk Model

The tangential velocity is modeled considering power losses due to the viscous drag of the blade. Thus, Johnson's formulation is dependent on the lift-to-drag ratio (c_l/c_d) of the blade. However, VS-PAERO leverages some assumptions presented by [20] to avoid the need to provide aerodynamic data of the blade. The tangential velocity is given by:

$$V_t(r) = \frac{(V_\infty + v_o)v_o \omega r}{(\omega r)^2 + (V_\infty + v_o)^2} + 2v_o \frac{c_d}{c_l} \tag{13}$$

where,

$$v_o{}^2 = \frac{v_i{}^2}{[1 + C_{\tilde{T}} ln(C_{\tilde{T}}) + (C_{\tilde{T}}/2)]} \tag{14}$$

The c_l/c_d ratio is modeled using two relations that combines the blade coefficients with the hover thrust coefficient ($C_{\tilde{T}} = T / (\rho_\infty A(\omega R)^2)$) and the hover power coefficient ($C_{\tilde{P}} = P / (\rho_\infty A(\omega R)^3)$).

$$\sigma c_l = 6 C_{\tilde{T}} \tag{15}$$

$$C_{\tilde{P}} = \frac{\sigma c_d}{8} + \kappa \frac{C_{\tilde{T}}{}^{3/2}}{\sqrt{2}} \tag{16}$$

Equation (15) represents the definition of a mean lift coefficient in which the entire blade is assumed the be working at, and σ is the blade solidity. The first term of Eq. (16) is the profile power coefficient for a constant chord blade with constant drag coefficient, and the second term is the hover induced power loss correct by the empirical factor κ [20]. According to [20], considering a linear inflow distribution the value of κ is ≈ 1.17, which is the value used in the VSPAERO code.

Given the inputs C_T, C_P, and RPM, it is possible to evaluate $C_{\tilde{T}}$ and $C_{\tilde{P}}$. From there, a simple rearragement of equations allows to estimate the c_d/c_l term present in Eq. (13) and compute the tangencial velocity.

2.3 Unsteady Analysis

One of the main objectives of the present work, as mentioned in section 1.2, is to evaluate the VSPAERO solver focusing on the actuator disk model. This model has the advantage of low computational effort at the cost of lacking some information about the flow field. For example, the actuator disk model does not provide the propeller's efficiency. Since C_T and C_P are inputs of this method, the propeller's efficiency must be known beforehand. Another limitation of the actuator disk model is that only the presence of the disk affects the wing's flowfield. Although, the wing's presence does not affect the propeller performance. In most cases, the wing's influence on the propeller can be neglected without much concern. According to [15], however, in some conditions, the two-way interference might be necessary to provide reliable predictions.

The VSPAERO has a second approach to model propellers, which is called the *Rotating Blades Mode*. It is an unsteady resolution of the flow field, where the propeller's blades are modeled as

rotating wings, and no prior knowledge about the propeller, besides the geometry, is needed. Therefore, this model can evaluate the blade efficiency, the C_T and C_P (instead of having them as inputs), at a given flight condition. Furthermore, the blade elements are also part of the linear system solved by the aerodynamic model, which means that, in this model, the propeller-wing interaction is taken into account. The downside is that it is a much more time-consuming method, and a proper time-step needs to be selected to have converged results in the steady-state.

Since the *Rotating Blades Mode* is used only in specific cases, it falls out of the scope here to enter more in detail about its formulation. However, according to [13], it is worthy to point out that, for low speed flows, the physical constraints on the vorticity distribution for the unsteady case are the same as the steady case. Also, the induced velocity at a given point by a vortex segment is not only a function of its position but is also a function of time ($\vec{V_i}(\vec{r},t)$). For more details, reference [13] has a complete dedicated chapter on this matter.

3. Methodology

This paper will present three different scenarios of analysis. The first one is the isolated wing, which will serve as a baseline for both model calibration and evaluation of the variation in CL and CD when in the presence of the different arrangements of propellers. The second scenario represents the typical cruise condition of the X-57, where only the wingtip-mounted propellers are on. For these two scenarios, a simple model of parasite drag integral is applied to enhance the wing's drag polar evaluation. The third scenario simulates the typical landing condition, where the 12 high-lift propellers are deployed while the wingtip propellers still operate to provide thrust.

The flow-field characteristics of the cruise (8000 ft) and landing (sea level) flight phases are summarized in Tab. 2.

Table 2 – Typical flight conditions for the X-57 "Maxwell". Cruise flight level at 8000 ft and 150 KTAS. Landing flight level at sea level and 58 KTAS.

Parameter	Symbol	S.I. units		Imperial units	
Cruise					
Velocity	V_∞	77.16	[m/s]	253.17	[ft/s]
Density	ρ_∞	0.96296	[kg/m^3]	0.001869	[slug/ft^3]
Reynolds Number	Re	2.7911e+06	[-]	2.7911e+06	[-]
Take-off/Landing					
Velocity	V_∞	77.16	[m/s]	97.82	[ft/s]
Density	ρ_∞	1.225	[kg/m^3]	0.002377	[slug/ft^3]
Reynolds Number	Re	1.3126e+06	[-]	1.3126e+06	[-]

The next sections will describe in more details each scenario, starting with the model calibration and mesh convergence, following to the parasite drag model (which improves the current model present in VSPAERO). Then, in the wingtip-mounted propeller section it will be discussed two approaches of evaluating the impact of the propeller installed in such position. Finally, it is presented the characteristics of the leading edge distributed propellers and some installation parameters, as rotor positioning and pitch, are discussed.

3.1 Mesh Convergence

Prior to initiate the study on how distributed propulsion (DP) parameters affects the wing's aerodynamics, it is necessary to calibrate the model settings and understand the VSPAERO best practices. This was done using the data available in the article "Comparison of Aero-Propulsive Performance Predictions for Distributed Propulsion Configurations" [6] as a benchmark.

In that article, the author presents a *pseudo-validation* of the "design-order" methods they used during the X-57 development. It is called a *pseudo-validation* because at the time the article was written, no experimental data were available, and they made comparisons with three different higher order CFD methods [6].

For the purposes of calibration of the aerodynamic model, the following results compares the data obtained via the OpenVSP model against the results from the "design-order" methods from [6]. So, to describe and compare the results against the other CFD results is beyond the scope of this section. The first step is to establish the mesh refinement that will provide the best balance between agreement with available data versus computational time. For this purpose, five different meshes were compared (Tab. 3).

Table 3 – Wing mesh characteristics. Simulation time refers to the time spent to simulate with a simple laptop computer with 16 Gb of RAM, and CPU Intel$^{\circledR}$ Core$^{™}$ i7-4510U @ 2.00GHz 2.60GHz with a 64-bit Windows 10 operating system.

Mesh	Kutta nodes	Chord-wise nodes	Simulation time
Coarse	16	5	2.0 s
Medium	26	15	5.2 s
Fine	51	31	25.5 s
Very Fine	101	61	2 min 47 s
Ultra Fine	201	123	19 min 9 s

Figure 4 clearly shows that a poorly refined mesh would lead to an underestimated C_{L_0}. A reasonable explanation for this behavior is that, with few chord-wise elements (which the "Coarse" mesh has only four), the wing camber surface will not represent its real shape and will possibly be a flat plate-like shape. On the other hand, the meshes with more chord-wise elements can better model the wing camber, improving the lift coefficient calculation. This also helps to understand why the results converged with the mesh refinement.

From Tab. 3 it is clear that the simulation time rapidly increases with mesh refinement. In addition, in Fig. 4 it is seen that the "Fine" mesh presents acceptable results when compared with those from Ref.[6] (named "Benchmark" in Fig. 4). Therefore, the "Fine" mesh is the choice for the next simulations of this work.

The span-wise mesh refinement is directly related to the induced drag (C_{D_i}) calculation. According to the results from Fig. 5, the mesh refinement had a minor effect on the drag portion which is dependent on the lift.

The shift from the VSPAERO results and the reference data is probably due to the parasite drag calculation. As a first estimation, the VSPAERO solver uses flat plate approximations, corrected with experimental data from the NACA 0012 airfoil to compute the parasite drag of the wing. For cambered airfoils, however, this approximation may not be acceptable depending on the level of fidelity expected from the results. In addition, in the "Benchmark" results, the parasite drag from the wingtip nacelles is considered. The next section will address an improved approach, the parasite drag integration analysis, which has shown better agreement with results from Ref.[6].
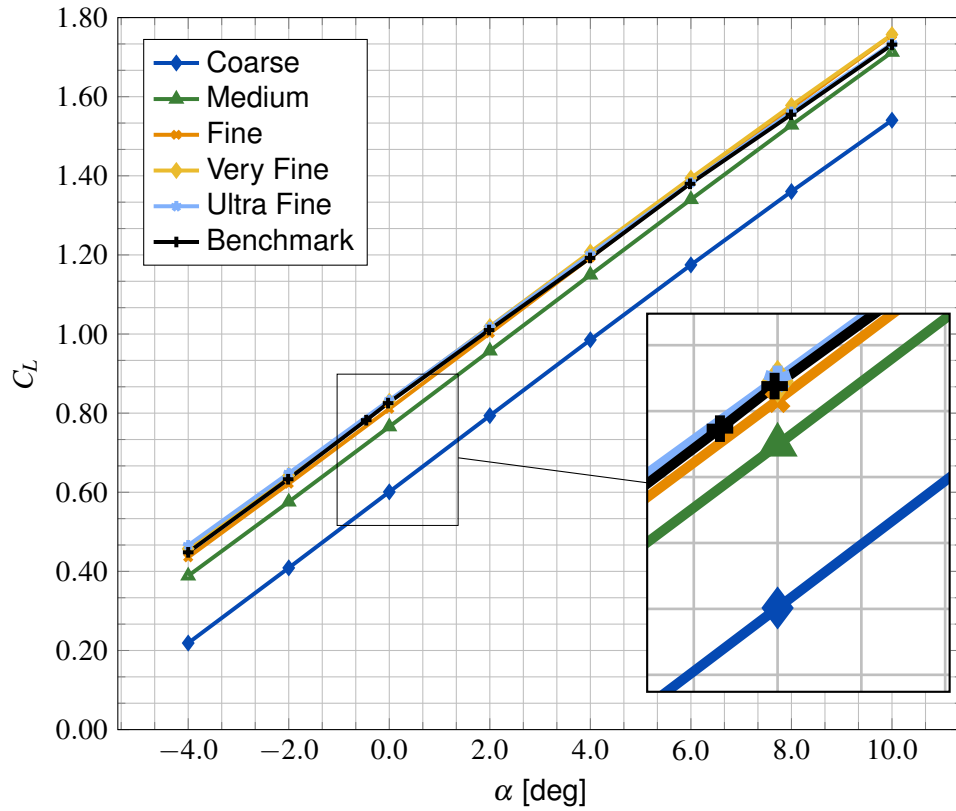
Figure 4 – C_L vs. α curve for different mesh resolutions. Simulation conditions: wing alone, $Re_\infty = 2791100$, eight α varying from -4° to 10°. Symmetry condition was applied.
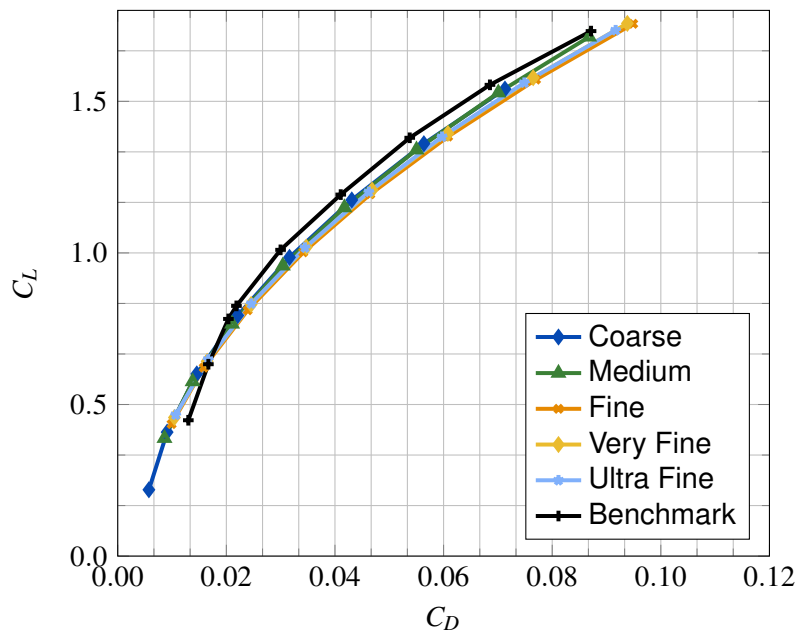
Figure 5 – C_L vs. C_D curve for different mesh resolutions. Simulation conditions: wing alone, $Re_\infty = 2791100$, eight α varying from -4° to 10°. Symmetry condition was applied.

3.2 Parasite Drag Integral

The approach chosen to model this drag component is through an integration of the wing section drag over the wing span [10].

$$C_{D_0} = \frac{2}{S} \cdot \int_0^{b/2} c_d \cdot c \cdot dy + \Delta C_{D_{misc.}} \tag{17}$$

where S is the wing reference area, c is the wing chord at each dy location and c_d is the local section drag corresponding to the local section lift coefficient (c_l). The $\Delta C_{D_{misc.}}$ is to account for miscellaneous drag sources, such as the presence of nacelles or other components.

In this approach, the c_d values comes from a database that can be conceived by either experimental data or by numerical values obtained via other methodologies. The 2D drag coefficient is such that: $c_d = f(c_l, Re)$, where Re is the Reynolds number of the flow field. The Re dependency is important to cover cases with different flow-field velocities and to account for cases with tapered wings, where each wing section has a different chord length and, consequently, different local Reynolds number.

For the present work, the 2D aerodynamic coefficients comes from an XFOIL [21] simulation (Tab. 4). It is worth mentioning that the interface of the XFLR5 [22] was used to call the XFOIL solver since it is a more user-friendly environment. Once the 2D database is created and the wing's lift distribution is known (via the VLM simulations), the values of c_d can be easily interpolated with respect to the local c_l, which leads this approach to have very low computational cost.

After the generation of the c_d database using XFOIL, the procedure described above was implemented in a MATLAB [23] algorithm to calculate the wing's parasite drag. It can be summarized by the following steps:

1. Import database from XFOIL and apply a filter to not consider the near stall data.

2. Data interpolation, so that c_l has a constant step. In this way, a c_d lookup table is defined where each column represents a value of c_l and each row represents a Re.

3. Import the wing load from the VSPAERO results.

4. Evaluation of local section c_d according to the corresponding c_l and Re.

5. Drag integration along the wing span (Eq. 17).

6. Addition of other parasite drag sources, if applicable (e.g. wing mounted nacelles).

Note that step two is not strictly necessary, but it facilitates the drag interpolation process.

Table 4 – XFOIL simulation settings.

Parameter	Value
Reynolds number	$2.25\text{e}+06 \leq Re \leq 3.30\text{e}+06$
Reynolds number increment	$0.105\text{e}+06$
Angle of attack	$-5.0° \leq \alpha \leq 20.0°$
Angle of attack increment	$0.25°$
NCrit	9.00
Forced transition	No
Viscous effects	Yes

As for the $\Delta C_{D_{misc.}}$ (see Eq. 17), it was considered the parasite drag from the wingtip nacelles, which was calculated with the Parasite Drag Tool [24]. This tool is based on the approach of flat plate skin friction coefficient, corrected by a form factor FF that estimates the pressure drag due to viscous separation. The estimated value of the parasite drag from the wingtip nacelles is 0.00168 and was summed to the wing parasite drag.

It is important to note that this methodology has some limitations. One of them is that the interpolation only works if the wing's local c_l and c_d are within the range of values simulated in the 2D database. For the leading edge distributed propellers case, this can be a drawback. The wing sections in the presence of the propellers experience higher dynamic pressure than they would without the blowing propellers. Then, since the lifting surface methods, including VSPAERO, normalizes the aerodynamic forces by the freestream dynamic pressure (q_∞), the local coefficients in this region become much larger than the 2D simulation. This limitation can be corrected if, before the interpolation process, the local coefficients are normalized with respect to the true local airspeed. Another limitation of this methodology, when applied to the wing in the presence of multiple propellers, is that it can not account for the drag component due to the interaction between the propeller's slipstream and the wing and with each other's.

3.3 Wingtip-mounted Propellers

To evaluate the performance of the wingtip-mounted propeller two approaches are considered. The first one is to get the direct results of lift and induced drag from the VSPAERO calculations, using the Actuator Disk mode, and then add the parasite drag with the methodology mentioned above. The second approach is to use the same hypothesis used by Ref.[6], which is based on the work of [8] and will be briefly commented next. All results are compared in section 4.2.

3.3.1 Miranda & Brennan Approach

Miranda and Brennan demonstrated that, given a constant load distribution along the wing span and constant power input, the effective efficiency of a tractor installation is the same as a pusher installation. Such demonstration was accomplished through a generalization of Munk's Stagger Theorem, illustrated in Fig. 6.
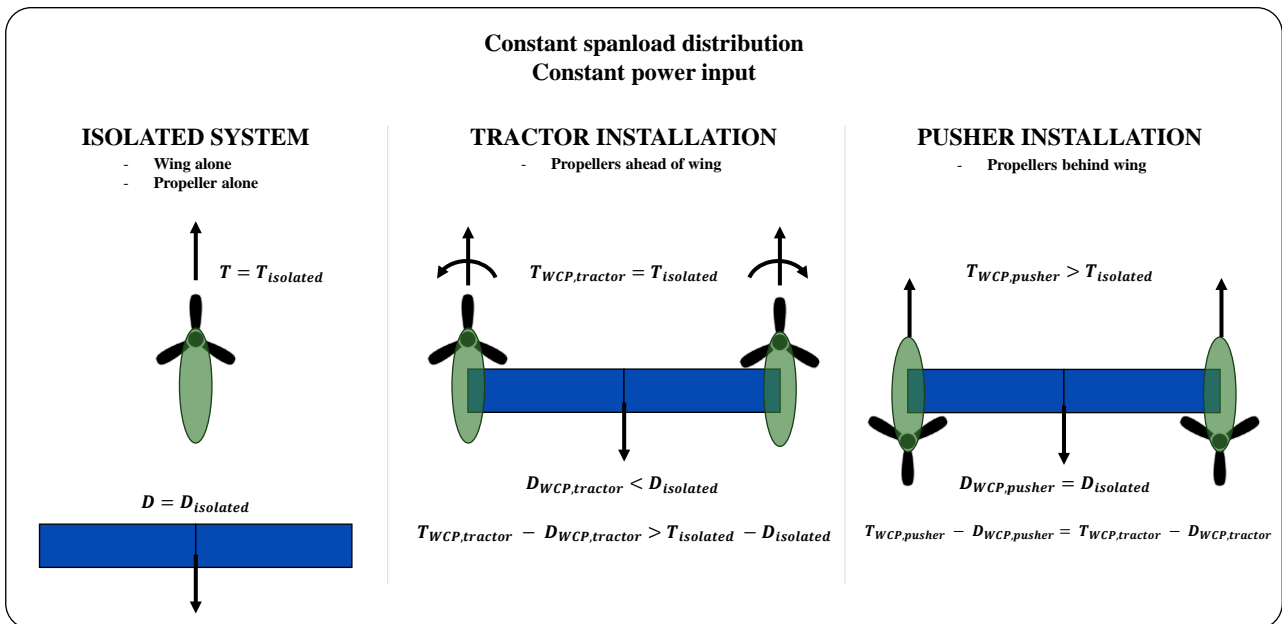
Figure 6 – Generalized Munk's Stagger Theorem. Reproduced and adapted from Ref.[8].

The fact that both installations have the same effective efficiency, at least under the assumptions of Ref. [8], means that the following equation holds:

$$T_{WCP,\text{pusher}} - D_{WCP,\text{pusher}} = T_{WCP,\text{tractor}} - D_{WCP,\text{tractor}} \tag{18}$$

where WCP refers to the configuration of the wing with the cruise propellers installed. Moreover, from Fig. 6 it can also be inferred that the propeller's efficiency (η) remains constant for the isolated and the tractor installation cases and that the pusher installation has a higher propeller efficiency. Note that the system/installation overall efficiency remains constant, but the propeller efficiency can vary.

In short, the conclusion of [8] is that a system with wingtip-mounted propellers will have a better performance than when these components are in isolation. Such improvement can be interpreted as a reduction in induced drag or as an increase in thrust, depending on the type of installation. The drag coefficient of the tractor installation ($C_{D_{WCP}}$) can be calculated from Eq. 19:

$$C_{D_{WCP},\text{tractor}} = C_{D_{WC},\text{isolated}} + \left(1 - \frac{\eta_{installed,pusher}}{\eta_{isolated}}\right) \cdot C_{D\text{tot}} \tag{19}$$

where $C_{D_{WC},\text{isolated}}$ is the total drag of the isolated wing with cruise configuration, $\eta_{installed,pusher}$ is the propeller efficiency when installed in the pusher configuration, $\eta_{isolated}$ is the isolated propeller efficiency, and $C_{D\text{tot}}$ is the aircraft total drag estimated to maintain unaccelerated flight.

It is important to understand that, even though the baseline aircraft has a tractor configuration, the pusher configuration is the one used in the simulations to evaluate the $C_{D_{WCP}}$. The reason for that is because through Eq. 19 it is possible to "decouple" the wing's total drag from the aircraft's total drag in a relatively simple manner. Actually, in some cases (during the initial design phase) it can be interesting to be able to work with both installations, regardless what the actual installation is, as shown by the case study of [6].

The advantage of the method presented above is that, once the propeller efficiency is known for the installed and isolated cases, one only needs the total drag of the isolated wing to compute the drag of the powered wing (given that both wing load and power input are constant). However, it is important to keep in mind its assumptions and validity. In the original formulation of Miranda and Brennan, they neglected the effect that the axial flow acceleration induced by the propeller has on the wing. The propeller slipstream contraction was also neglected. They also stress out that "...the present theory is a theory of given distributions of aerodynamic forces rather than the solution of an aerodynamic flow for a given set of boundary conditions" [8].

So, in order to verify how these assumptions can impact the results, three unsteady simulations were conducted with VSPAERO. The idea is to use a more complex method, within the software capabilities, and then compare what the differences. The unsteady simulations modeled the three systems installations: isolated, tractor, and pusher.

Looking into Fig. 7a one can see that the presence of the propeller in the rear position of the wing, in the pusher configuration, causes a small depreciation in the wing loading towards the wing tip. However, the distribution remains fairly similar case where the wing is in isolation. Then, it is reasonable to assume that the isolated wing and the pusher configtiuration will produce similar drag force, as sugested in Fig. 6. As for Fig. 7b, it shows clearly that the isolated and the tractor systems will have similar propulsive efficiency, whereas the pusher configuration will indeed be the most efficient one. Therefore, the method provided by [8] is appropriate for initial evaluations in early design phases.
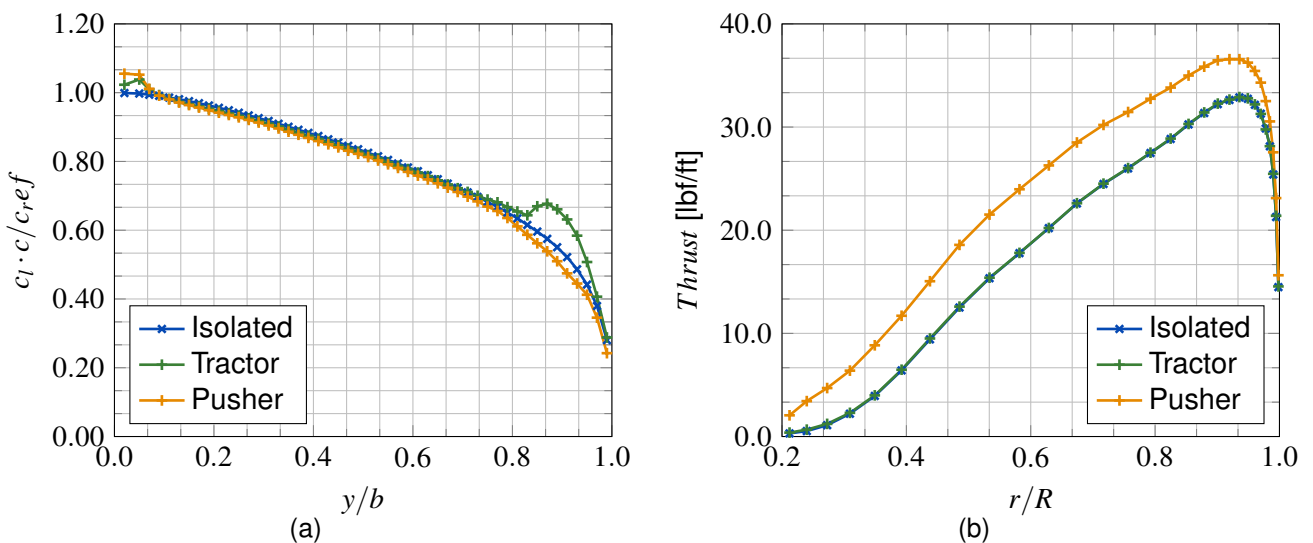
Figure 7 – (a) Wing loading; (b) Blade loading. Comparing the isolated, tractor and pusher systems, at typical cruise flight conditions.

The simulation results shown in Fig. 7 where also used to calculate the efficiency parameters needed in Eq. 19. They are: $\eta_{isolated}$=0.86177; η_{pusher}=0.90437; $\eta_{tractor}$=0.86332; and $C_{D_{tot}}$=0.06153. Note that the $C_{D_{tot}}$ is based on the total thrust calculated by the simulation, so the cruise condition would be in equilibrium.

3.4 Leading Edge Distributed Propellers

The next paragraphs will briefly discuss the difference between the design goals of a blade optimized for thrust and one optimized for lift augmentation, which is important to understand how the Actuator Disk Model described in section 2.2 will affect the expected results. Then, it will be presented a study of different parameters that can influence the efficiency of the DP system in generating extra lift. All the good practices regarding mesh refinement and model settings in VSPAERO, established in the previous sections, are maintained here.

3.4.1 Different Propeller Blade Designs

The main goal of the high-lift propellers is to increase the dynamic pressure over the wing and, therefore, increase the total lift. This means that an optimum blade in this scenario is not the one that produces more thrust (design focus on Minimal Induced Loss - MIL), but it is the one with the most uniform axial velocity profile (most efficient in blowing the wing). This difference of objectives introduces major changes in the design process of the blade [3], and results in different blade geometries. High-lift propeller blades usually have increased chord lengths and twist angles near the root, and near the middle of the blade chord lengths and twists decreases [6]. For comparison, Fig. 8 illustrates the differences between the chord distribution of a propeller blade design to maximize thrust and another the maximizes the uniformity of the induced axial flow. Reference [25] provides a rich level of details on the X-57 high-lift propellers geometry and performance.
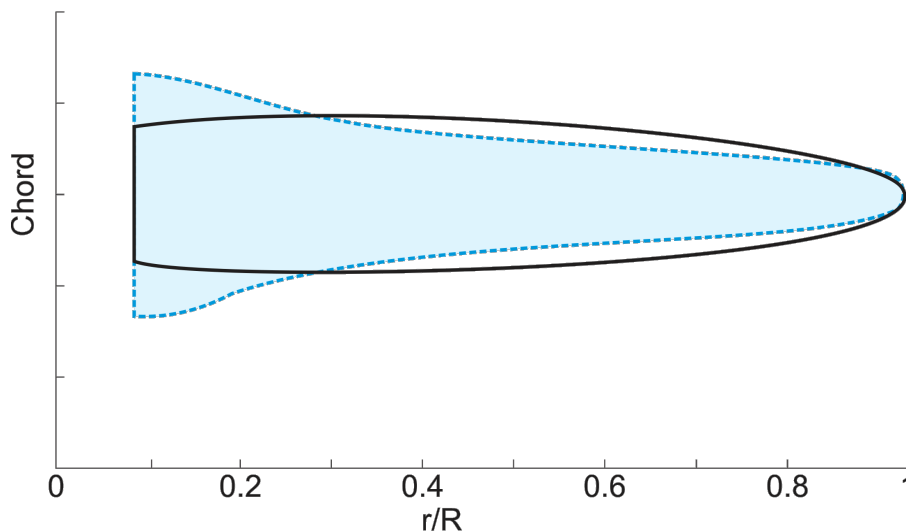
Figure 8 – Chord distribution of a high-lift propeller blade (dashed line) and a blade optimized for thrust (solid line). Adapted from [6].

Figure 9 shows the distribution of induced axial velocity for both types of blades. Note that, as described earlier, the high-lift blade has a flatten curve, while the one optimized for thrust has a peak around 3/4 of the blade's radius.

An elliptic distribution is also shown in Fig. 9, which is the one adopted by VSPAERO's actuator disk model. It is important to consider this when analyzing the DP results. For example, since an elliptical distribution is being modeled, depending on the propeller position, this could mean that the results of lift augmentation are somewhat conservative. In other words, the elliptical modeling will privilege configurations with Z near the wing, as there is a loss of velocity near the blade tip. Furthermore, Fig. 9 also illustrates that real blades might have a hub, which does not contribute to the induced axial velocity. Note that for both high-lift and MIL propellers, the velocity distribution begins near 25% of
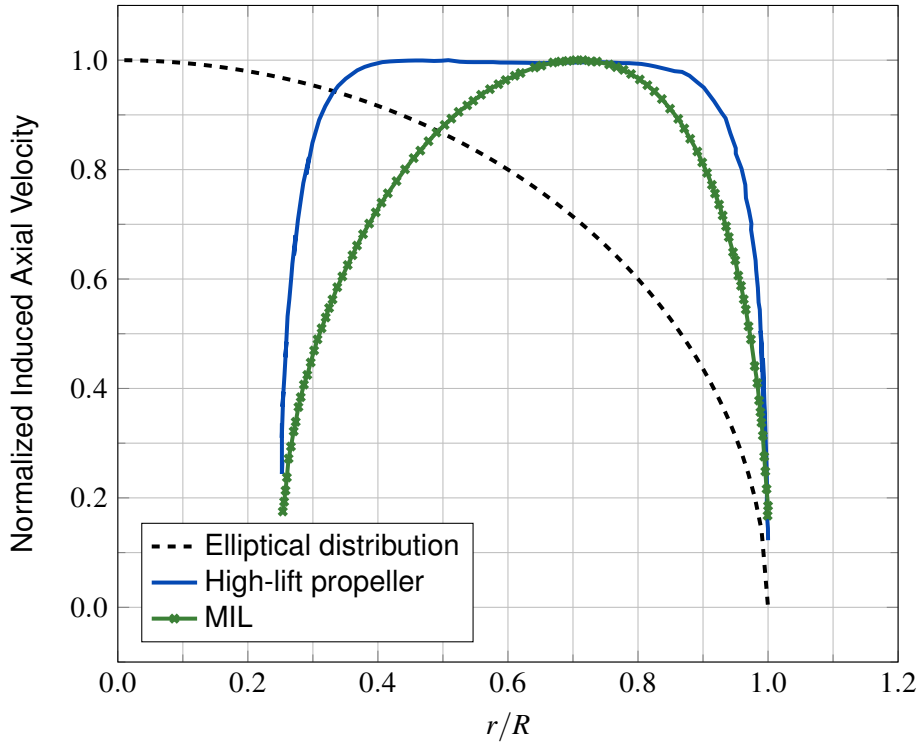
Figure 9 – Axial induced velocity distribution of a high-lift propeller blade (dashed line), of a blade optimized for thrust (solid line), and an elliptical distribution.

the blade radius. This characteristic can be modeled in VSPAERO's actuator disk model by setting the hub's diameter, and it should be a point of attention.

The distributions from Figures 8 and 9 are only illustrative and does not represent actual distributions from existing projects.

3.4.2 Parametric Study

The X-57's leading edge distributed propellers are usually deployed in low-speed flight phases, to improve the lift generation at such conditions. For this reason, all analysis considering the complete set of DEP will be at sea level and 58 KTAS (knots, true air speed), as shown in Tab. 2.

At this conditions, Ref. [25] provides the expected performance of the high-lift propeller (see Fig. 10) for a given operational range. These were the values of C_T, C_P and RPM considered for the VSPAERO simulations. Since the considered velocity is constant, the RPM can be evaluated from the advance ratio definition:

$$J = \frac{V_\infty}{(\text{RPM}/60).D}$$

$$\therefore \quad \text{RPM} = \frac{60.V_\infty}{J.D} \tag{20}$$

The use of DEP enables a whole new set of design parameters, which are usually "constant" in conventional propulsive configurations. Therefore, evaluating some of these parameters is relevant to a better understanding of wing designs with DEP.

Here it will be evaluate changes in the propeller's Z position (Z_p), X position (X_p), and the propeller pitch (Θ). The next paragraphs will explain how these parameters were modified. Important to notice that for all analysis, the wingtip-mounted propellers are not modified, only the high-lift propellers are. However, they are considered to account for their impact in the lift distribution.

Propellers Z position

The first parameter is the propeller Z position, with the convention signs shown in Fig. 17. The Z_p
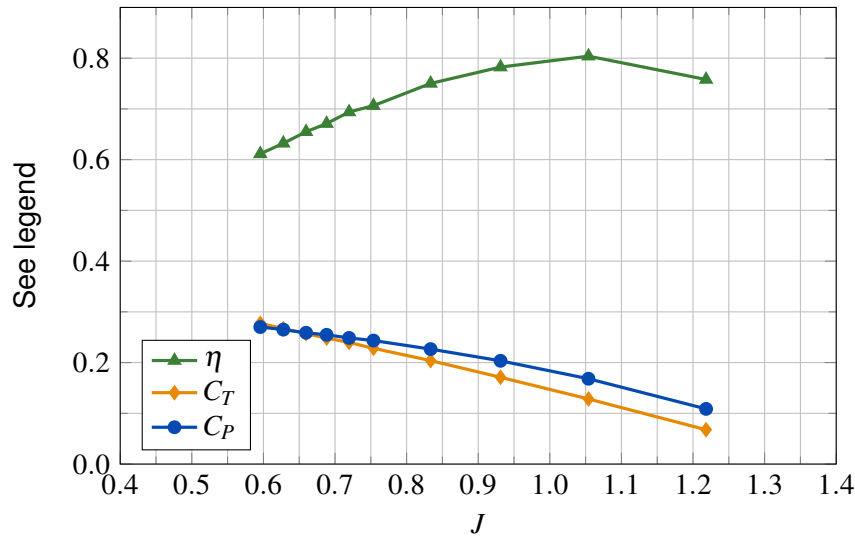
Figure 10 – High-lift propeller performance parameters modeled with XROTOR at $V_\infty = 58$ KTAS. Source: [25] .

values considered are: $-1R$, $-0.5R$, $-0.37R$ (design value), 0 (aligned with the root leading edge), $+0.5R$, and $+1R$. Where R is the radius of the high-lift propellers (0.945 ft).
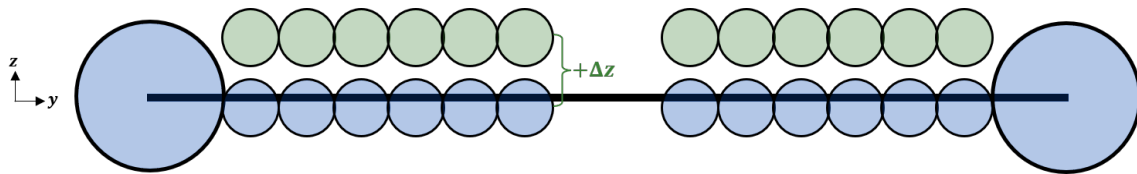
Figure 11 – High-lift propeller Z_p position, and coordinate reference.

The change in Z_p modifies the portion of the wing washed-out by the rotor slipstream. For the elliptic loaded propeller, modeled in VSPAERO, it is expected that for positions where the center of the rotor is distant from the wing they will present worse performance in terms of lift augmentation.

Propellers X position

For the analysis of X_p, instead of using absolute values, as in the Z_p case, it was considered variations from the design point (ΔX_p) (see Fig. 19). The reason of this choice is that the X-57 rotors have a staggered placement and, to consider an individual change in each rotor would result in a vast trade-space domain. By adopting a Δ to the whole group, the problem is simplified.
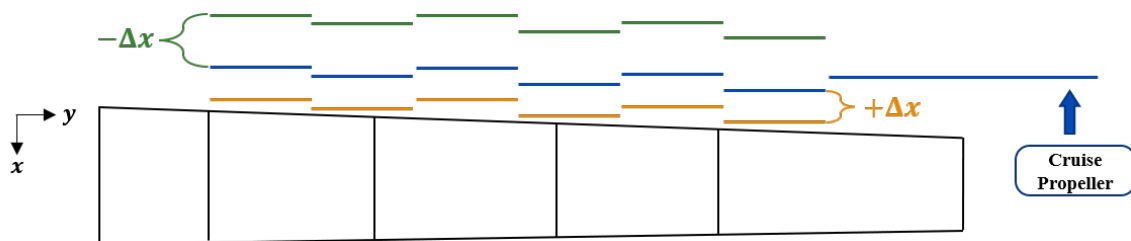
Figure 12 – High-lift propeller X_p position, and coordinate reference. A positive change ΔX moves the high-lift propeller group in the aft direction of the wing.

The evaluated values of ΔX_p are: $-1R$, $-0.5R$, $-0.25R$, 0 (design value), $+0.25R$, and $+0.5R$.

Propellers pitch

Finally it will be analysed the effect that the propeller's pitch (Θ) has in the lift augmentation provided

16

by the DP system. It is a parameter of interest because it directly affects the effective angle of attack perceived by the wing section. Although low angles are usually considered in rotor installations, for this analysis the pitch angles evaluated are: -10°, -5°, 0° (reference), +5°, and +10°. It should be noted that the propeller pitch angle in the X-57 is not zero, and here this value is only used as a reference point.
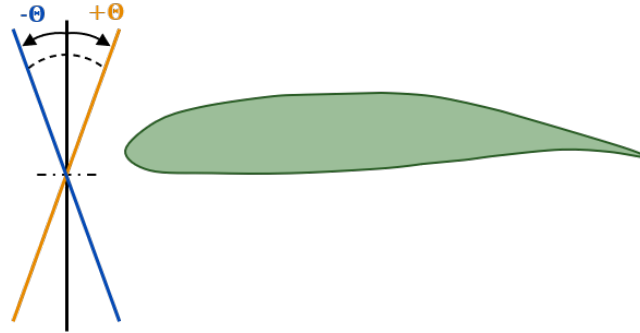
Figure 13 – Illustration of the sign convention used to define the propeller's pitch angle Θ.

4. Results and Discussions

4.1 Isolated Wing

Using VSPAERO to analyse an isolated wing, with conventional geometry is straight forward and provides reasonable results. As mentioned in section 3.1, for this case the mesh with best compromise between "accuracy" and computational time has 51 nodes in the spanwise direction and 31 in the chord-wise direction.

The results shown in Fig. 14 refers to the cruise flight condition. In Fig. 14a it is compared the results from Ref.[6], the estimations from the VSPAERO, and the results from the methodology described above. Note that the Drag Integration method improved the drag polar results when compared to the raw data from VSPAERO. It is seen that for C_L values that correspond to lower values of α (see Fig. 14b) there is a very good agreement with the "Reference" C_D. Such agreement was expected, seeing that the reference values were obtained from similar methodology as presented here (although they used different software). It is worthy to recall that these results take into account the parasite drag for the wingtip nacelles.
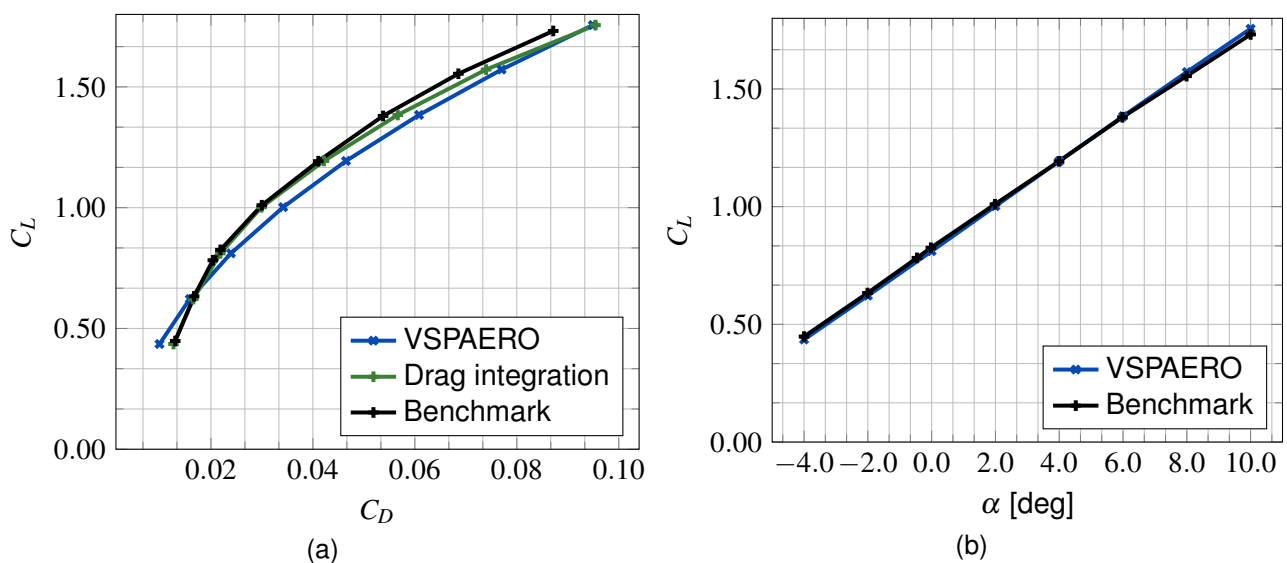
Figure 14 – (a) Drag polar comparing different methodologies; (b) C_L vs. α comparing the VSPAERO results with Ref. [6].

4.2 Wingtip-Mounted Propellers

For the wing at cruise configuration (WCP) two approaches were considered to evaluate the effect of the propellers installed at the wingtip. From Fig. 15 it is evident the improvement of the wing performance in the presence of propellers configuration. The solid lines represents the polar of the wing with the cruise powered condition, whereas the dashed lines are the polar for the wing alone. Figure 15 also supports the argument made above that the Miranda & Brennan's approach would have similar results with the ones directed obtained via the VSPAERO simulations. Despite having an offset from the reference results, it can still be considered that theses results are satisfactory. The curves behavior are similar, and the offset indicates a minor discrepancy with the C_{D_0} evaluation.
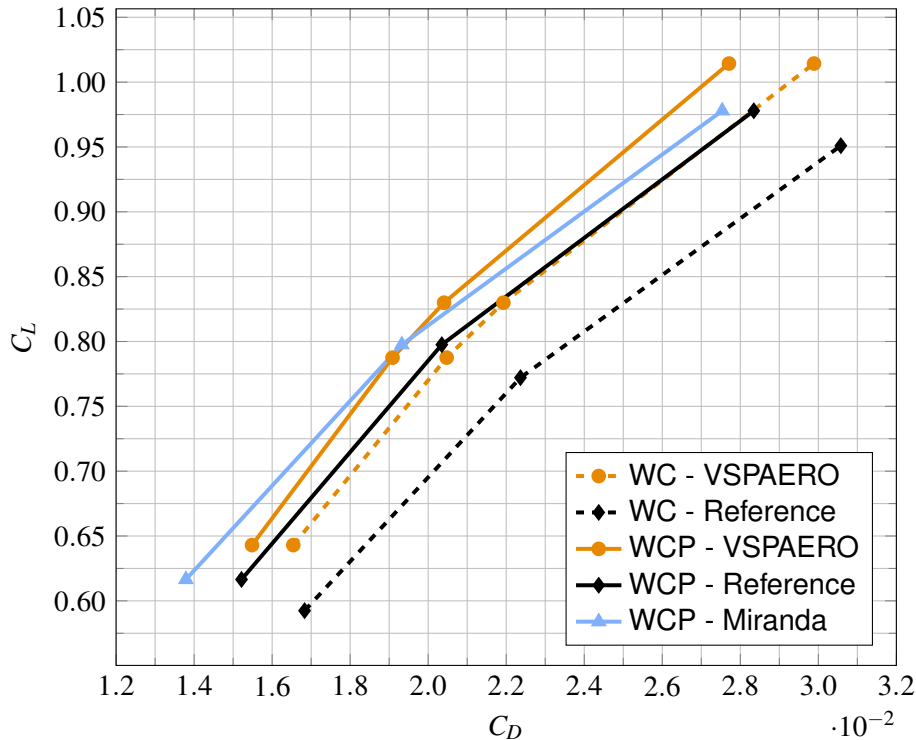
Figure 15 – Drag polar comparison of wing alone (WC) and the wing with operating propellers (WCP).

4.3 Leading Edge Distributed Propellers

The typical operational procedure of the X-57 in cruise phase, is to operate only with the wingtip motors, and the high-lift propellers are conformally folded along the nacelles to reduce drag [25]. The high-lift propellers are only deployed at low-speed flight phases, such as take-off and landing, where more lift coefficient is required to balance the aircraft's weight.

Usually, when evaluating low-speed flight phases, the wing's aerodynamic characteristics are presented considering flap deflection. The X-57 has a Fowler flap able to extend up to 30°. However, this represents a condition likely to have detached flow at moderate angles of attack, and it is also a complex geometry to be modeled as a lifting surface. To consider the flapped wing for this case, using the "VLM" mode of VSPAERO, is a condition that may not be adequate for the method's assumptions and, therefore, would not produce reliable results. Also, since one of the goals of this work is to evaluate how VSPAERO captures and models the effects of the propellers on the wing, there is no reason to add external empirical corrections, such as presented by [26], to consider the effects of flaps. In other words, the presented results will reflect only the result of the VSPAERO modeling, and corrections to consider a $\Delta C_{L_{flap}}$ can be added later on, if necessary. For these analysis, the good practices of mesh refinement and model settings found by the former cases are maintained here.

The reference flight condition for all results are at sea level, 58 KTAS. The cruise propellers were considered to operate at 2100 RPM with $C_T = 0.2294$, $C_P = 0.2165$. The high-lift propellers reference operation are at 4550 RPM with $C_T = 0.250$, $C_P = 0.2555$. The simulations that consider a range of

the high-lift propellers operation point, follow the values provided in Tab. 5, which are base on the data from Fig. 10 [25].

Table 5 – High-lift propeller performance data. Source: [25].

J	RPM	C_T	C_P
0.596	5216.9	0.2773	0.2701
0.648	4550.0	0.2499	0.2555
0.754	4122.8	0.2282	0.2435
0.931	3337.1	0.1710	0.2035
1.218	2550.7	0.0677	0.1088

Propellers Z position

   The Z_p position effect on increasing the dynamic pressure is closely related to the propeller's blade loading. If the most part of the wing is exposed to a region lightly loaded, the propeller blowing will have a minor effect. This consequence is captured by the VSPAERO model, as shown in Fig. 16 for the cases where Z_p is one radius below or above the wing the lifting coefficient curve approaches the curve from the wing without the high-lift propellers, only with the cruise propellers (WCP). Whereas, for Z_p values where the rotor center has a close alignment with the wing, the lift augmentation effect is more evident.
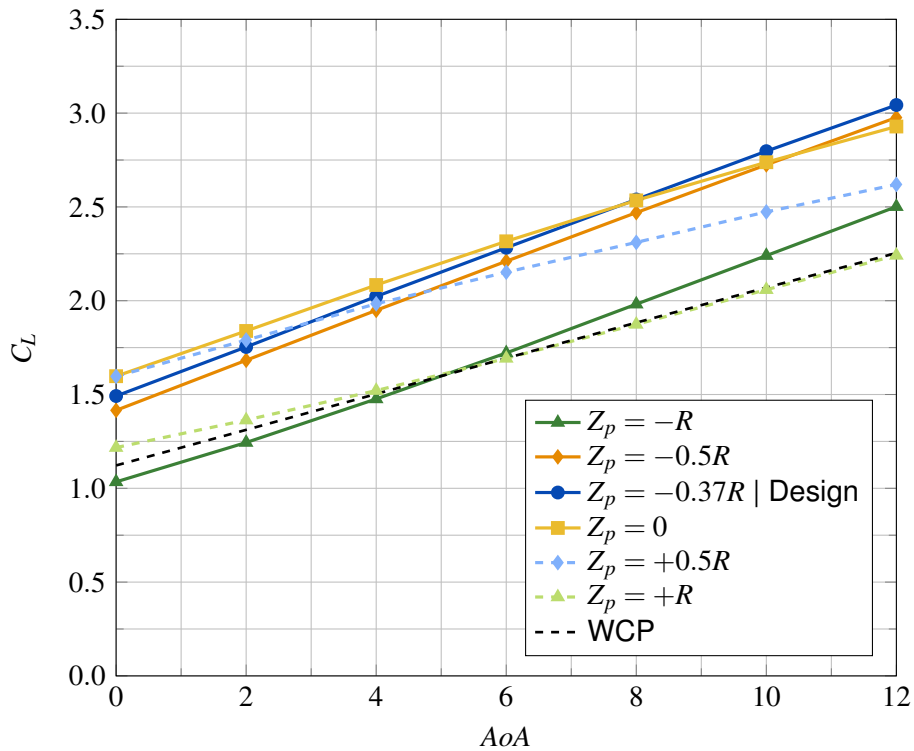
Figure 16 – C_L x α for the high-lift propellers in different Z_p positions.

Figure 17 provides a new perspective to evaluate the different Z positions. It shows that for lower advance ratios, Z_p will have a pronounced effect on the wing lift. At higher values of J, this difference becomes smaller, as well as, the lift augmentation effect. Which was the expected behavior, since at a constant speed and rotor diameter, a higher advance ratio translates to lower RPM and, therefore, less air is blown towards the wing.

Propellers X position

   The results of changing the rotors X position are consistent with the expected behavior from the

(a) $\alpha = 0°$

(b) $\alpha = 12°$
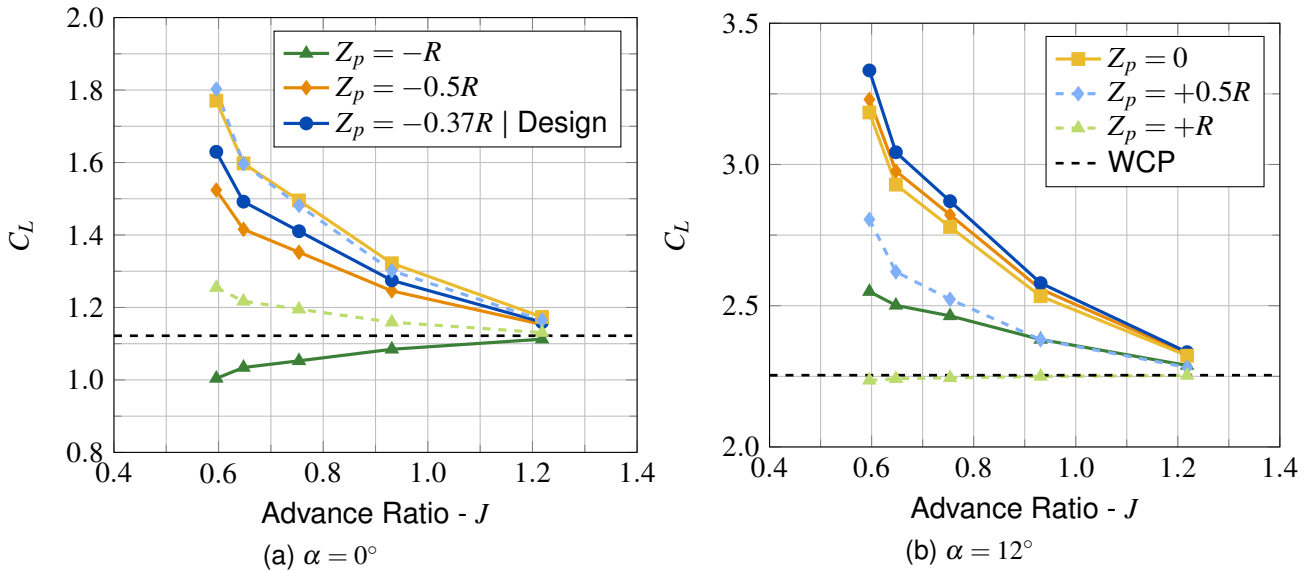
Figure 17 – C_L values for different Z_p position at different high-lift propeller operating points, at constant angle of attack.

literature, where further positions upstream provide better lift augmentation [3, 6]. However, according to the findings of [6], the propeller's X position upstream of the wing should have more impact on the lift coefficient, mainly due to the propeller slipstream contraction, and this is not observed in the results shown in Figures 18 and 19.

This difference could indicate that a wider range of ΔX_p values should have been considered. Another possibility is that the assumptions of the actuator disk model described in section 2.2 do not properly model the high-lift propeller's slipstream contraction. Further work is in progress to evaluate both possibilities.
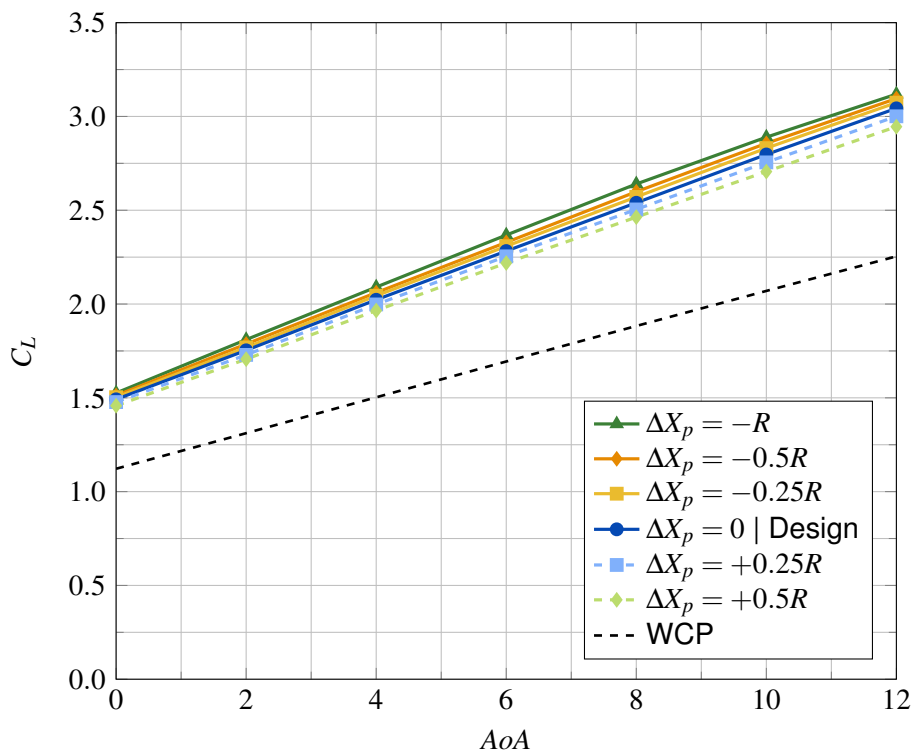
Figure 18 – C_L x α for the high-lift propellers in different ΔX_p variations.
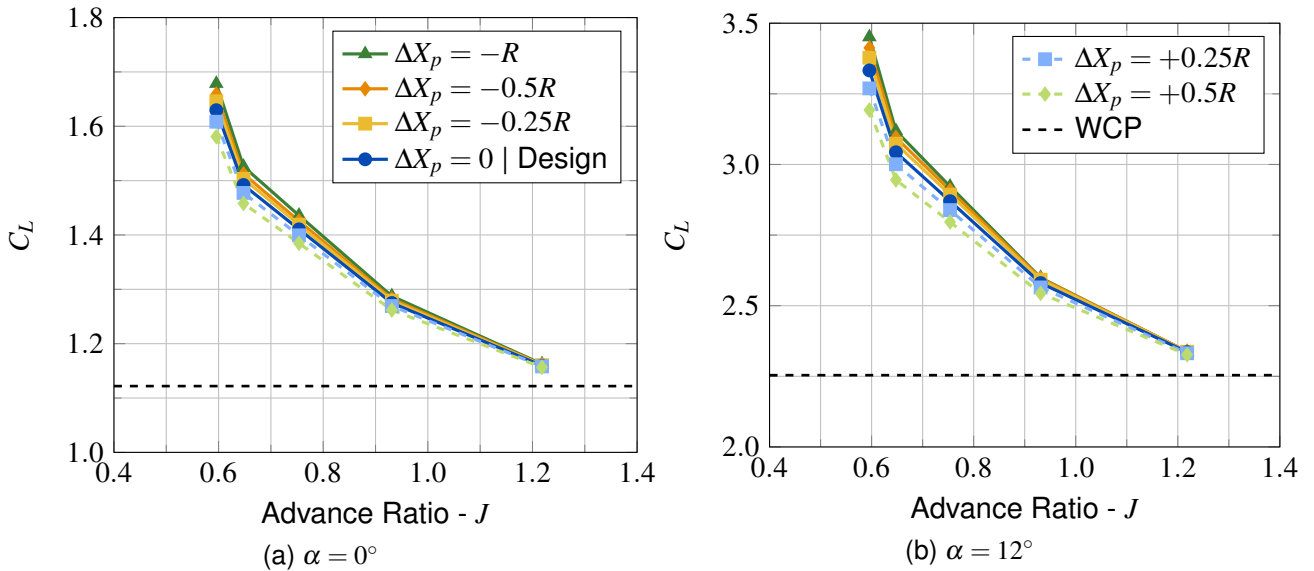
Figure 19 – C_L values for different ΔX_p variations at different high-lift propeller operating points, at constant angle of attack.

Propellers pitch

According to [3], it is reasonable to have high-lift propellers with moderate negative pitch angles since they only operate in low-speed regimes, namely, at high angles of attack. This configuration would allow the rotor to be aligned with the freestream at such conditions.

Figure 20 shows that each pitch angle provides an almost constant ΔC_L. When analyzing Eq. 4 from section 2.1, it is clear that the velocity induced by a given rotor enters as an external velocity component and will act to change the effective angle of attack at each wing section washed-out by that rotor. Therefore, the negative pitch angles increases the effective α, improving the lift augmentation effect.
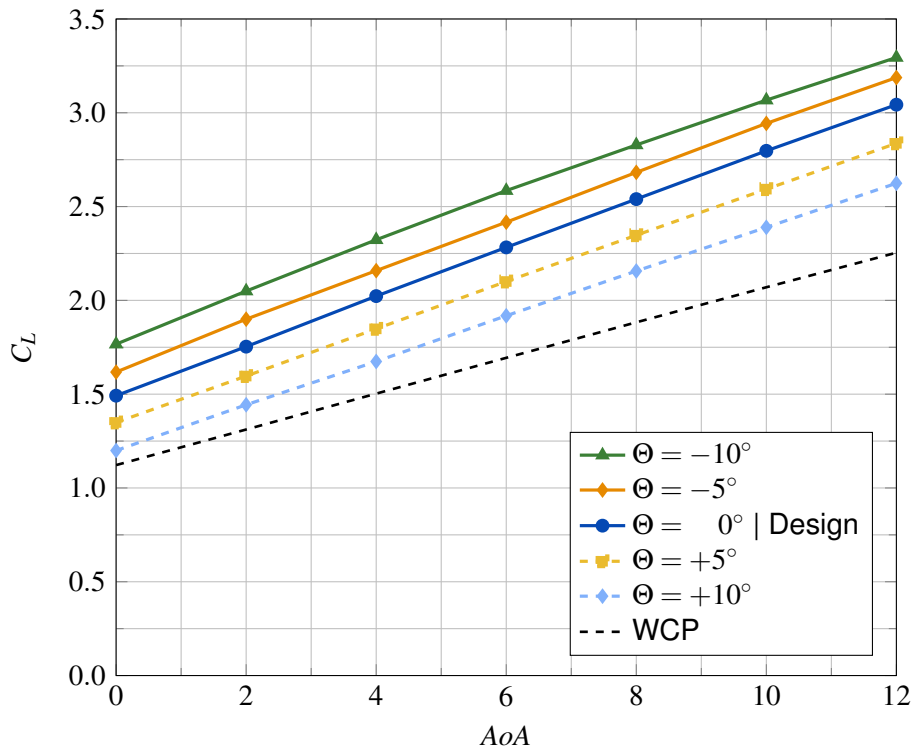
Figure 20 – C_L x α for the high-lift propellers in different Θ angles.

Figure 21 shows a similar pattern to Fig. 17, where the lift augmentation is magnified at lower advance ratio conditions, and mitigated at higher values of J. It is reasonable to say that this behavior occurs because at high RPM, the change in the effective α will be more pronounced, whereas at low RPM, this change will be smaller, approximating the results of the wing int he WCP configuration.
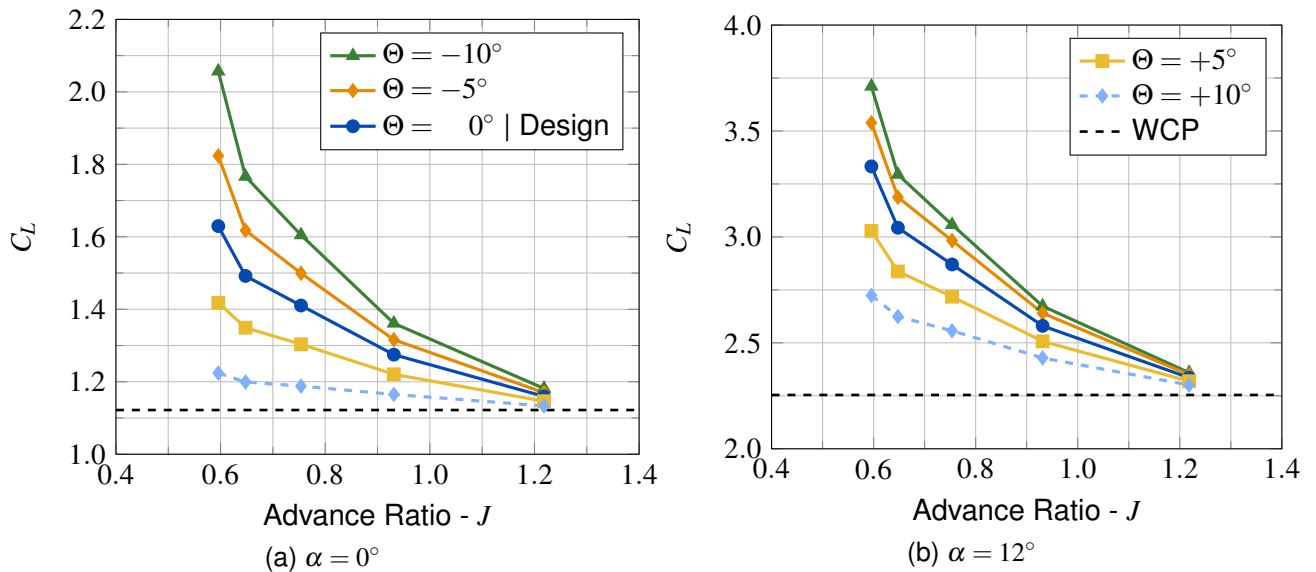
Figure 21 – C_L values for different Θ angles at different high-lift propeller operating points, at constant angle of attack.

5. Next Steps and Concluding Remarks

The proposed methodologies have shown satisfactory results. The *Parasite Drag Integral* method enhanced the raw data from VSPAERO for the case of the isolated wing. Regarding the simulations with the WCP configuration, some of the simplifications assumed by Miranda and Brennan were confronted against the VSPAERO unsteady simulations for the propeller blades. The impacts of its simplifications and assumptions were evaluated and showed little influence in the final results.

The simulations with all 14 rotors at a low-speed regime, have shown reasonable results. Most of them are in agreement with what was expected from the literature. Thus, the capabilities of VSPAERO to model complex external flows might be considered appropriate. In addition, together with the OpenVSP power to model parametric geometries, these consists of a powerful suite of applications to support early phase designs.

However, as in any other engineering software, the user must be aware of the applied methods to understand the range of validity of its results and to judge if the outputs are conservative or if they are optimistic.

Future developments of the present work will include an improvement to the *Parasite Drag Integration* to be able to model the parasite drag under more complex flow conditions. In addition, it is on the road-map to evaluate the propeller-wing interference on each other using the unsteady mode available in VSPAERO.

6. Copyright Statement

References

[1] Arthur Dubois, Martin van der Geest, JoeBen Bevirt, Sean Clarke, Robert J Christie, and Nicholas K Borer. Design of an electric propulsion system for sceptor. In *Aviation Technology, Integration, and Operations Conference*, 2016.

[2] Alex M Stoll, JoeBen Bevirt, Mark D Moore, William J Fredericks, and Nicholas K Borer. Drag reduction through distributed electric propulsion. In *14th AIAA aviation technology, integration, and operations conference*, page 2851, 2014.

[3] Michael Dobson Patterson. *Conceptual design of high-lift propeller systems for small electric aircraft*. PhD thesis, Georgia Institute of Technology, 2016.

[4] OpenVSP. OpenVSP Main Page, 2021.

[5] Nicholas K Borer, Michael D Patterson, Jeffrey K Viken, Mark D Moore, JoeBen Bevirt, Alex M Stoll, and Andrew R Gibson. Design and performance of the nasa sceptor distributed electric propulsion flight demonstrator. In *16th AIAA Aviation Technology, Integration, and Operations Conference*, page 3920, 2016.

[6] Nicholas K Borer, Joseph M Derlaga, Karen A Deere, Melissa B Carter, Sally Viken, Michael D Patterson, Brandon Litherland, and Alex Stoll. Comparison of aero-propulsive performance predictions for distributed propulsion configurations. In *55th AIAA Aerospace Sciences Meeting*, page 0209, 2017.

[7] Nicholas K Borer and Marty Kelsey. Nasa's x-57: Learn how electric is the shape of things to come. Available at: `<https://www.youtube.com/watch?v=6FYn6O5t1L4&ab_channel=SmithsonianNationalAirandSpaceMuseum>`.

[8] Luis Miranda and J Brennan. Aerodynamic effects of wingtip-mounted propellers and turbines. In *4th Applied Aerodynamics Conference*, page 1802, 1986.

[9] OpenVSP. VSP Hangar, 2021.

[10] Ira H Abbott and Albert E Von Doenhoff. *Theory of wing sections: including a summary of airfoil data*. Dover, New York, 1959.

[11] John David Anderson. *Fundamentals of aerodynamics*. Tata McGraw-Hill Education, New York, 5 edition, 2010.

[12] John J Bertin and Russell M Cummings. *Aerodynamics for engineers*. Pearson Education Limited, Courier Westford, 6 edition, 2014.

[13] Mark Drela. *Flight vehicle aerodynamics*. MIT press, 2014.

[14] Barnes W. McCormick. *Aerodynamics, Aeronautics, and Flight Mechanics*. Pearson Education Limited, USA, 2 edition, 1995.

[15] Leonardus Louis Maria Veldhuis. *Propeller wing aerodynamic interference*. PhD thesis, Delft University of Technology, 2005.

[16] Tomas Sinnige. *Aerodynamic and Aeroacoustic Interaction Effects for Tip-Mounted Propellers: An Experimental Study*. PhD thesis, Delft University of Technology, 2018.

[17] David Kinney. 2020 VSP WS: VSPAERO Theory, Validation, and Features. Available at: `<https://www.youtube.com/watch?v=-zQEmmrb6ck&t=941s&ab_channel=OpenVSPVideos>`, 2020.

[18] Joseph Katz and Allen Plotkin. *Low-speed aerodynamics: from wing theory to panel methods*. McGraw-Hill, Incorporated, 1991.

[19] John T Conway. Analytical solutions for the actuator disk with variable radial distribution of load. *Journal of Fluid Mechanics*, 297:327–355, 1995.

[20] Wayne Johnson. *Helicopter theory*. Dover Publications, 1994.

[21] H. Drela, M.; Youngren. Xfoil v6.94, 2000.

[22] Andre Deperrois. Xflr5 v6.43, 2018.

[23] The Mathworks, Inc., Natick, Massachusetts. *MATLAB version 9.9.0.1467703 (R2020b)*, 2020.

[24] OpenVSP. Openvsp, 2020.

[25] Brandon L Litherland, Nicholas K Borer, and Nikolas S Zawodny. X-57 maxwell high-lift propeller testing and model development. In *AIAA AVIATION 2021 FORUM*, page 3193, 2021.

[26] Daniel Raymer. *Aircraft Design: A Conceptual Approach*. American Institute of Aeronautics and Astronautics, Inc., Reston, 6 edition, 2018.